Nickel Nitride Particles Supported on Two-dimensional Activated Graphene-Black Phosphorus Heterostructure: An Efficient Electrocatalyst for the Oxygen Evolution Reaction

Xiao Wang, Qiaoxia Li, Penghui Shi, Jinchen Fan[a,b]*, Yulin Min[a,b]*,Qunjie Xu[a,b]*

[a]*Shanghai Key Laboratory of Materials Protection and Advanced Materials in Electric Power, Shanghai University of Electric Power, Shanghai 200090, P. R. China*

[b]*Shanghai Institute of Pollution Control and Ecological Security, Shanghai200092, P.R. China*

E-mail: Jinchen.fan@shiep.edu.cn; ahaqmylin@126.com; xuqunjie@shiep.edu.cn;

Abstract

Hydrogen is regarded as the most promising green clean energy in the 21st century. Developing the highly efficient and low-cost electrocatalysts for oxygen evolution reaction (OER) is of great concern for the hydrogen industry. In the water electrolyzed reaction, the overpotential and the kinetics are the main hurdles for OER. Therefore, an efficient and durable oxygen evolution reaction electrocatalyst is required. In this study, an activated graphene (AG) – black phosphorus (BP) nanosheets hybrid is fabricated for supporting Ni_3N particles (Ni_3N/BP-AG) in the application of OER. The Ni_3N particles are combined with the BP-AG heterostructure via facile mechanical ball milling under argon protection. The synthesized Ni_3N/BP-AG shows excellent catalytic performance toward the OER, demanding the

overpotential of 233 mV for a current density of 10 mA cm^{-2} with a Tafel slope of 42 mV dec^{-1}. The Ni$_3$N/BP-AG catalysts also show remarkable stability with a retention rate of the current density of about 86.4% after measured for 10,000s in potentiostatic mode.

Key words: black phosphorus, graphene, nickel nitride, oxygen evolution reaction, heterostructure

1 Introduction

Along with the development of society, the gradual exhausted of fossil fuels has become a major puzzle. The problem has brought the intense pursuit of highly efficient and sustainable energy conversion and storage means, among which electrolyzed water for hydrogen has been regarded as one of the most capable approaches [1]. As a half reaction of electrocatalytic water splitting, oxygen evolution reaction (OER) usually demands around 1.8-2.0 V to overcome the reaction obstacle which is mainly related to the dull transfer rate generated by complex electron redox process [2]. Electrocatalysts as key components play important roles in OER. At present, Ir/Ru-based catalysts are deemed as the top-priority selection for OER. Nevertheless, the high cost and shortage of resources seriously hinder their large-scale application [3]. The probe of noble-metal-free electrocatalysts is born at the right moment.

Graphene as a two-dimensional crystal has received great attention due to its excellent electrical, optical and mechanical properties. Owing to its large surface area and high electro conductivity, graphene is constantly considered as ideal building blocks for metal or non-metal catalysts [4]. Mai *et al*. [5] developed graphene as the supports for the Metal–organic framework derived carbon-confined Ni$_2$P nanocrystals. The catalysts show superior electrocatalytic performance than that of the commercial IrO$_2$. Ishihara *et al*. [6] prepared nitrogen-doped

graphene to prop up Ni-Fe nitride nanoplates for reversible OER. Chen *et al.* [7] exploited nitrogen and sulfur-codoped graphene composites with Co_9S_8, which can work for H_2 and O_2 in the same electrolyte. In the past decades, the researcher explored various types of graphene-supported hybrids for OER to take the place of noble metal catalysts. On this basis, 2D/2D heterojunctions which possess rich, active sites, low intrinsic resistance and convenient transport path [8] have been investigated simultaneously.

In this regard, the other graphene-like 2D materials have been diffusely inspected both experimentally and theoretically. However, due to the no direct bandgap of graphene, the logic switching of semiconductors cannot be realized, which restricts the application of graphene in the semiconductor field and photovoltaic field. However, the low mobility of two-dimensional transitional metal dichalcogenides (TMDs), such as MoS_2 and WS_2, with direct bandgap also limits their application in the territory of electronics [9]. Therefore, it is especially important to find two-dimensional materials with suitable bandgaps and great conductive capability. Fortunately, black phosphorus (BP) come to light which pulls double duty.

Similar to graphene, black phosphorus is a stabilized crystal with the corrugated layer structure. Because of its combination of van der Waals forces, the black phosphorus can be peeled easily off into single or few layers [10]. In the monoatomic layer, each phosphorus atom forms the pleated honeycomb structure, which consists of the covalent bond with the adjacent three phosphorus atoms by sp^3 hybridization. Phosphorene (black phosphorus with a single atomic layer thickness) is a natural p-type semiconductor [11, 12]. When the valence band electrons jump vertically to the conduction band, the electron wave vector does not change accordingly. Therefore, it has a direct band gap, and the band gap can be controlled by the number of layers in the range of $\sim$0.3 eV (about 30 layers) to $\sim$1.5 eV (single layer) [11-13]. Moreover, it shows obvious anisotropy, and the elastic modulus in the x-direction and the effective mass of the crystal electrons are small, which makes the black phosphorus with high

electron mobility. Furthermore, the electron mobility of the single layer black phosphorus can reach 10^4 cm^2 / (V·s) [14].

In general, BP is widely used in the field of photocatalysis because of its adjustable band gap. Previously, Yu *et al*. [15] showed a black-red phosphorus heterostructure as visible-light-driven photocatalysis synthesized by a simple ball milling method. Majima *et al*. [16] demonstrated that the BP/ graphitic carbon nitride was used as a photocatalyst for H$_2$ evolution invisible to near-infrared region. The photoelectric effect of few-layers BP nanosheets has been fully revealed. On the other hand, electrocatalytic performances of pure few-layers BP nanosheets for OER were reported to testify further implementation [17].

Except for spacious surface areas and admirable electron conductivity, luxuriant edge sites play a vital role in the catalytic process [9, 18]. As is known, transition metal nitrides may befittingly absorb between the surface of nitrides and the protons due to the characteristic electronic structure. At the same time, plentiful active sites render transition metal nitrides emerge as one kind of highly efficient electrocatalyst for hydrogen generation [19]. Vaidhyanathan *et al*. [20] established benzimidazole COF supported Ni$_3$N as the catalyst for OER oxidizes alkaline water with a topping low overpotential of 230 mV @ 10 mA cm^{-2}. Chen *et al*. [21] designed cobalt nickel nitride nanowires which were self-supported for overall electrochemical water splitting.

Based on the above discussion, we put forward a rational way to build the graphene-black phosphorus hybrids for supporting Ni$_3$N to enhance the OER activity. Through simply ball-milling process, the graphene activated through KOH (AG) is rationally combined with BP and Ni$_3$N. The results demonstrated that the Ni$_3$N/BP-AG demonstrates not only high OER activity with low overpotential, but also benign stability in alkaline condition. The Ni$_3$N/BP-AG shows better advantages than the commercial Ru-based and Ir-based OER catalysts. Hence, we have reason to believe that the Ni$_3$N/BP-AG will have great potential in electrocatalyst for OER.

2 Results and Discussion

### 2.1 Characterization of Ni$_3$N/BP-AG Catalysts

In this paper, the activated graphene (AG) was obtained by commercial pristine graphene nanosheets which were originated from mechanical exfoliation of graphite activated by 6 M KOH [22]. BP was prepared by ball-milling red phosphorus.Moreover, Ni$_3$N particles were gained *via* the reported method. First, NiCl$_2$•6H$_2$O reacts with NH$_4$F and urea in a hydrothermal reaction to form precursor. Then the green precursor was heated at 380°C for 2 hours under the NH$_3$ atmosphere to produce the Ni$_3$N particles [23]. As illustrated in **Scheme 1**, the preparation of AG/BP hybrids was achieved through ball milling of AG and BP with the high pressure and temperature under engorged argon protection. After that, the as-prepared Ni$_3$N was transferred into the jar for further ball-milling. Finally, the catalyst was indexed as Ni$_3$N/BP-AG-1 according to the mass ratio of Ni$_3$N: BP: AG = 1: 1: 1.
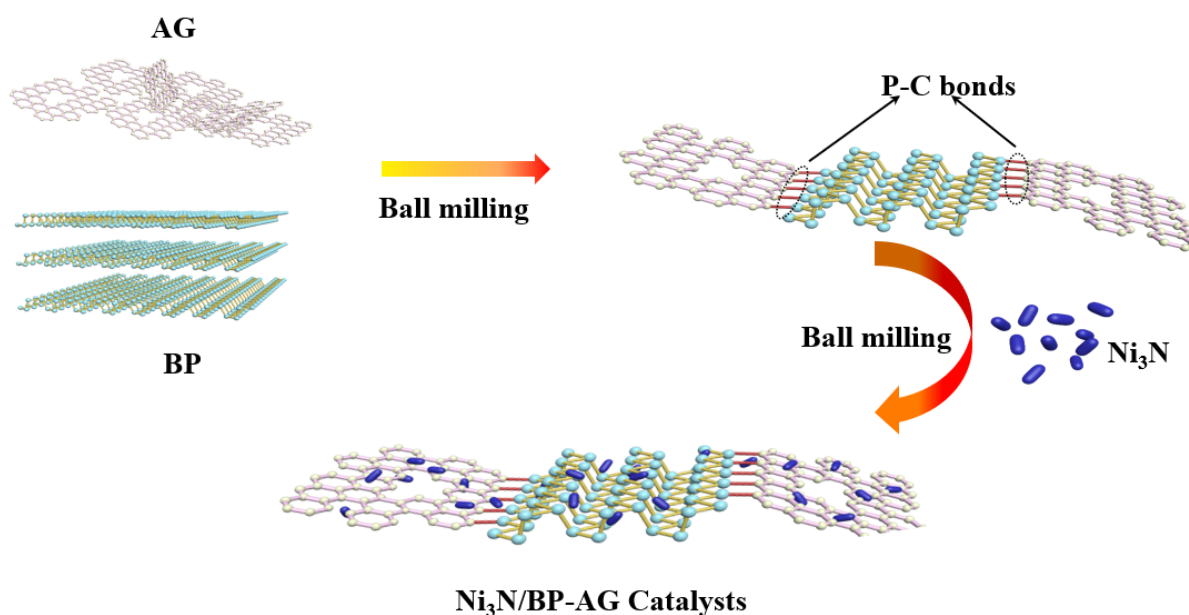
Scheme 1. Schematic illustration of the fabrication of the Ni$_3$N/BP-AG hybrids.

Figure 1a shows X-ray diffraction (XRD) patterns of the BP, AG, Ni$_3$N, BP-AG, and the Ni$_3$N/BP-AG-1 hybrids, respectively. Following the standard XRD pattern of orthorhombic BP (JCPDS No. 73–1358), BP gained by ball milling pattern owns the emblematic peaks at 2θ=15°, 33.5° and 55.6°[15], which suggests the existence of black phosphorus with small crystal size. The diffraction peak at 25.6° in AG is consistent with the plane of graphite (002)[22]. All the diffraction peaks support that the crystalline structure of hexagonal Ni$_3$N with purity phases indexes well to the hybrids (according to the JCPDS 10-0280, a=b=4.621 Å; c=4.304 Å) while ball milling with the BP and AG. Moreover, the diffraction peaks of the Ni$_3$N (111), (002), (110) and (112) planes in the patterns of the Ni$_3$N/BP-AG-1 hybrids are weaker than those of the pure Ni$_3$N, which may owe to the doping of P species in the crystal lattice of partial Ni$_3$N particles. This result may be same as the circumstance of the weak C peak at 25.6° in BP-AG. In addition, the diagnostic peaks of BP cannot be presented distinctly in the XRD pattern of Ni$_3$N/BP-AG hybrids, which could be attributed to the reaction process accompanied with the oxidation of few-layer BP and destruction caused by the generation of P-C bonding and formation of P$_x$O$_y$ during the individual reaction [24, 25]. And the basement would be more stabilized because of the P-C bonds[22]. From the inserted Raman spectrum of **Figure 1**b, Raman peak located at 362 cm^{-1} can be assigned to the A$_g^1$ mode, while peaks at 440 and 467 cm^{-1} are conforming to the in-plane B$_{2g}$ and A$_g^2$ modes of commercial BP bulk, respectively [26]. By contrast, the peaks of as-prepared BP nanosheets by mechanical exfoliation are transferred to lower wavenumber for about 13, 9 and 3 cm^{-1}, which may be ascribed to the degeneration of BP nanosheets with the decrease of thickness in consistent with the previous analysis [17]. **Figure 1**b also plots a typical Raman spectrum of the BP-AG. Except for the D peak, the significant G peak of graphene appears distinctly. In addition, this consequence hints the component combined with BP are few layers [27]. Extra, the I$_D$/I$_G$ with a spectacular intensity ratio ~2.1 is attributed to the edges of nanosheets and the appearance of a large

number of structural defects within the chips, which is in favor of the exposure of active sites[28]. It is fairly well known that along with the ball milling process, the defects of BP nanosheets are amplified. And the lifted edges are produced correspondingly.
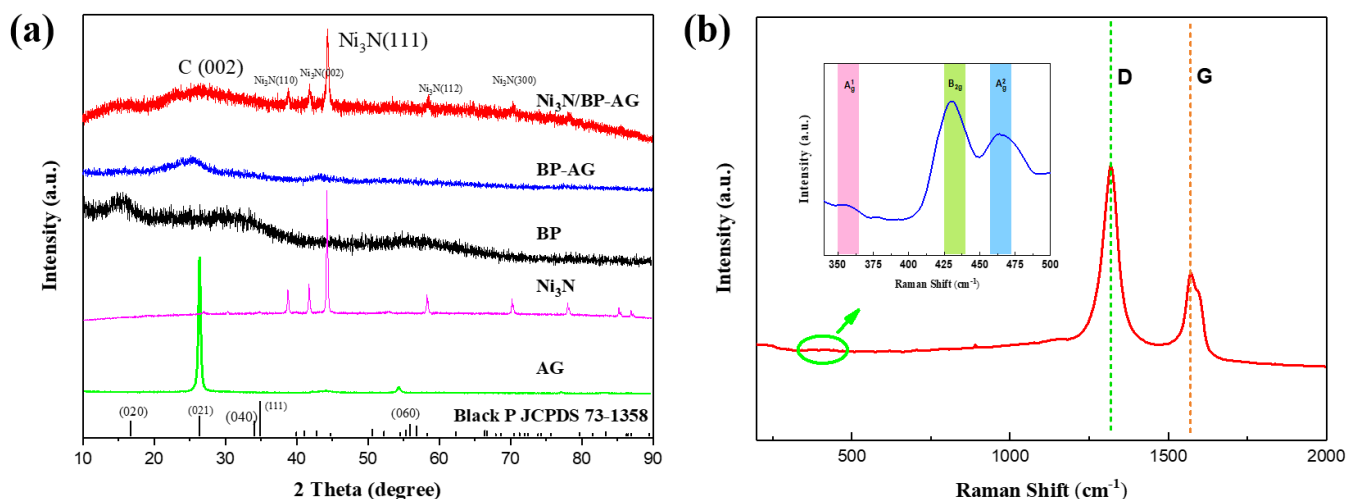

Figure 1. (a) XRD patterns of BP, AG, Ni_3N, BP-AG and Ni_3N/ BP-AG, (b) Raman spectra of BP-AG (Inset of (b): Raman spectra of BP).

The AG nanosheets can be seen clearly in **Figure 2**a. Under the electron irradiation, the graphene is nearly transparent. From the inserted image of **Figure 2**a, the thin AG nanoflakes with about 6∼8 layers can be seen clearly. According to Yu *et al*. [15], the BP which can be gained via easy ball milling red phosphorus is shown in **Figure 2**b. **Figure 2**c is the amplifying image of **Figure 2**b. It shows the representative TEM image of laminar BP nanosheets. By attention to this inset, the edge of BP confirms that the nanosheets are about 6 layers and the performance of less layers BP is better than bulk BP for OER[9]. As shown in **Figure 2**d, the characteristic lattice distance of 0.26 nm is in keeping with the (040) faces of BP. The cross-sectional atomic force microscopy (AFM) images as shown in **Figure S1 (**Supporting Information) demonstrate that the standalone BP is about 3.4 nm, which echoes the result of the former. Besides, the results further indicate that the integrated layer structure of BP nanosheets has been generated and retained during the ball milling process. In other words, the lamellar BP

nanosheets with characteristic structure has been gained. From the TEM image of **Figure 2**e, f, there is a distinct boundary of AG and BP from the AG-BP heterostructure. One side, the curved lattice fringes with as the characteristic of graphene can be seen obviously. The lattice distance of 0.34 nm is putting down to the C (002) flat interplanar spacing of AG. And the other side, the conterminous BP with (040) faces can be found. From the boundary between AG and BP, the AG-BP heterostructure is positively built. Therefore, compared to single substance, the active sites and charge transfer in AG-BP for direct activation of molecular oxygen and substrate are improved because of the heterojunction effect [8, 29]. Furthermore, the situation of $Ni_3N/BP-AG-1$ hybrids can be probed from **Figure 3**a. Compared with the previous AG, the $Ni_3N/BP-AG$ nanosheets became opaque due to the loading of BP and Ni_3N. In the high resolution TEM images (**Figure 3**b, c), the symbolization of Ni_3N particles were represented by the lattice fringes with the interplanar distance of 0.21 nm. And the distance is corresponding well to (111) planes of Ni_3N. This result shows that Ni_3N particles are present on the BP-AG heterojunction substrate. As witnessed from **Figure 3**d and **Figure S2**, energy dispersive spectroscopy (EDS) analysis indicated that BP and AG combined well with the Ni_3N particles which were distributed uniformly.
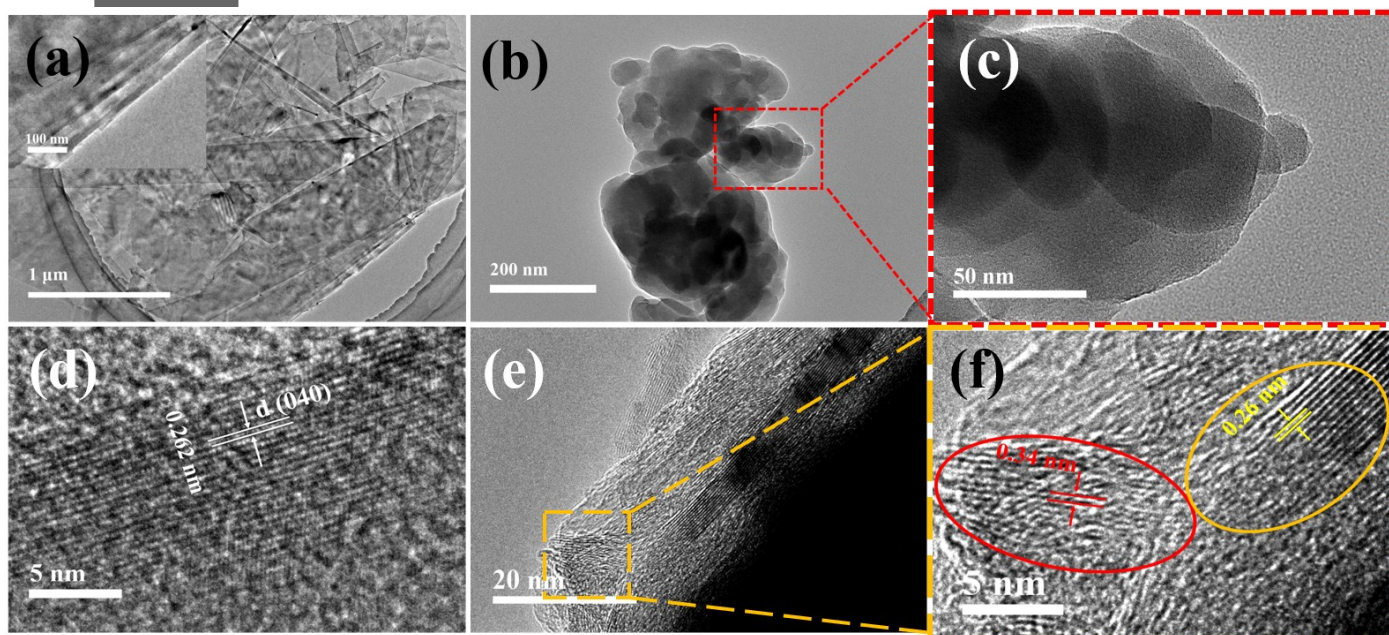
Figure 2. (a) TEM image of AG, (b, c) TEM image of BP, (d) HRTEM image of BP and (e, f) HRTEM image of BP-AG.

The electronic structure and surface information of Ni$_3$N/BP-AG-1 hybrids were explored by X-ray photoelectron spectroscopy (XPS). The characteristic peaks of C 1s, N 1s, P 2p, Ni 2p, and O 1s are shown in **Figure 4**a, respectively. For checking the peak shifts, the standard C 1s peak at 284.6 eV is selected as a reference and the O signal is from the surface oxidation. For Ni$_3$N/BP-AG-1 hybrids sample (**Figure 4**b), the appeared peaks located at ~856.9 eV and ~874.8 eV are attributed to the Ni 2p$_{3/2}$ and Ni 2p$_{1/2}$, respectively. The quite strong respond is corresponding to the Ni^{2+}. This result confirms the existence of Ni-P bonds [30]. Meanwhile, the peak located at 853.2 eV can be assigned to Ni$^+$ in Ni$_3$N. Identically, the N atoms were successfully boned with the Ni atoms according to the main characteristic peak centered at $\sim$ 398 eV which could be observed in the high-resolution N 1s XPS spectrum (**Figure 4**e). On the other hand, the sectional Ni$^+$ and Ni^{2+} could be oxidized into NiO and NiOOH, respectively. The NiOOH can be further oxidized into NiOOO* as the active sites [19, 23]. It is assumed that OER is a four-step electron transfer process involving the formation of intermediates *OH, *O, *OOH and O$_2$ [23, 32], and the surface Ni sites are considered to be the adsorption sites for binding oxygen intermediates [31]. As we know, the largest reaction barrier is determined by the maximum rate-limiting energy barrier. And this barrier is from the formation of *OOH in the reaction. Interestingly, even though the step before the formation of *OOH is spontaneous for Ni$_3$N, the large energy barrier value in the formation of *OOH also limits the progress of the reaction. However, in the catalyst, both of NiO and Ni$_3$N are present. Therefore, the result may imply the existence of coupled nano-interface between NiO and Ni$_3$N with optimized surface electronic structure during the reaction which can reduce the energy barrier in the rate-limiting step [31].
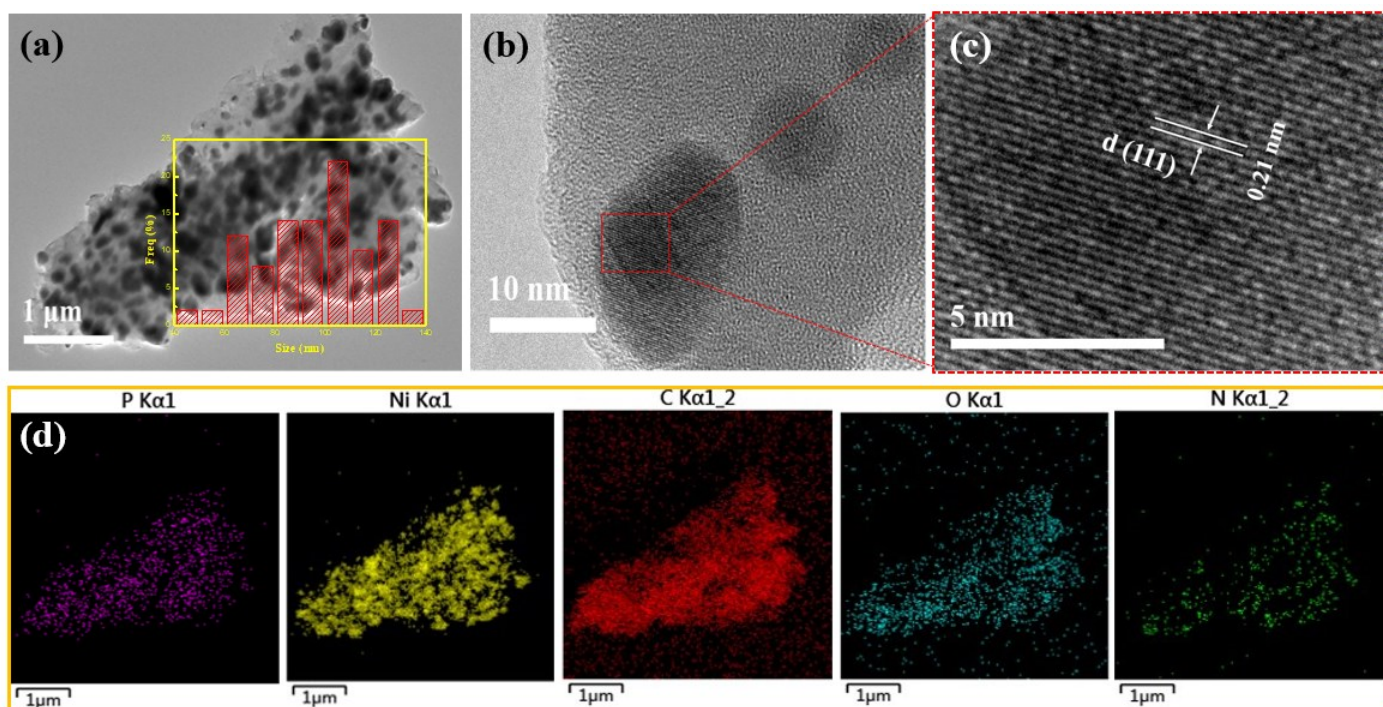
Figure 3. (a) TEM image of Ni_3N/BP-AG-1, (b, c) HRTEM image of Ni_3N/BP-AG-1, and (d) EDS mapping images for P, Ni, C, N and O elements in Ni_3N/BP-AG-1. (Inset of (a): Size distribution of Ni_3N particles on the surface of the BP-AG support.)

Furthermore, **Figure 4**c displays the high-resolution P 2p XPS spectra, and the peaks stand for the P $2p_{3/2}$ and P $2p_{1/2}$ are positioned on 130.02 and 130.81 eV, respectively, which can confirm the presence of phosphorus-phosphorus bonds derived from $BP^{[22, 24]}$. The reflection focus on ~134.4 eV uncovers the formation of the most prevalent phosphorous oxides (P_xO_y). As shown in **Figure 4**b, c and **Figure S3**, it is noteworthy that the peaks reveal shifts to higher BE by 0.9 eV for P-O and 0.4 eV for P 2p, lower BE by 0.6 eV for Ni 2p (133.5 eV for P-O, 129.6 eV for P $2p_{3/2}$, 130.4 eV for P $2p_{1/2}$, 857.5 eV for Ni $2p_{3/2}$ and 875.4 eV for Ni $2p_{1/2}$, [18, 19, 22, 26]) in Ni_3N/BP-AG-1. The augment of BE indicates the weak electron density screening effect due to the decrease of the electron density. Oppositely, the decrease illustrates the enhancement of electron density[32]. On this side, a point can be inferred. First, the electrons move from P to the interface of Ni_3N/heterostructure, and then, from Ni_3N/ heterostructure to

Ni sites. This transformation leads to the higher shifts of P 2p and lower BE shifts of Ni 2p

As for the generation of robust P-C bonds in the course of ball milling, the peaks of 130.46

131.68 eV [22] are ascribed to the representative reflection of P $2p_{1/2}$ and P $2p_{3/2}$ from the

generated P-C bond. Besides that, the evidence of ~283.5 eV [22] can be found from **Figure**

Therefore, the structural stability of the AG-BP substrate can be improved due to the diverse

interfaces between BP and AG. At the same time, the jarless construction promotes the

and contact between the exposed reaction sites and electrolyte on the OER process in an

alkaline condition.

In addition, the peaks of C 1s XPS in **Figure 4**d conform to the bonds of C-C/C=C, C-C.

And the O-C=O bond is found extra because of the oxidation of heterostructure surface. This

bond that embraces oxygen atoms can be accessorial reaction sites for the evolution of O_2 [19].

As illustrated in **Figure 4**e, the emblematic peaks located at 398.8 eV, 400.1 eV and 401.2 eV

can be divided into the pyridinic-N, pyrrolic-N, and graphitic-N, respectively. In this respect,

partial N atoms are doped into the graphene during the reaction [33]. At the same time, the N

atoms may become a bridge connecting the Ni_3N and the heterojunction substrate. This

creates complete channels for electron transport in the OER process on the Ni_3N/BP-AG-1

body.
2.2 Electrocatalytic performances

The electrocatalytic oxygen evolution reaction (OER) activities of the obtained samples

have been verified in an alkaline condition. At first, a three-electrode configuration had been

used to examine the catalytic activities of the compounds for OER in O_2-saturated 1.0 M

KOH with the catalyst loading of 254.78 μg cm^{-2}. In order to initially explore the optimal

ratio of catalysts, there are several kinds of mass ratio had been selected. Here, three types of

catalysts are revealed. Those are Ni_3N: BP: AG = 2: 1: 1 (Ni_3N/BP-AG-2), 1: 1: 1

(Ni_3N/BP-AG-1) and 0.5: 1: 1 (Ni_3N/BP-AG-0.5), respectively. And all potentials in this

paper are based on RHE.
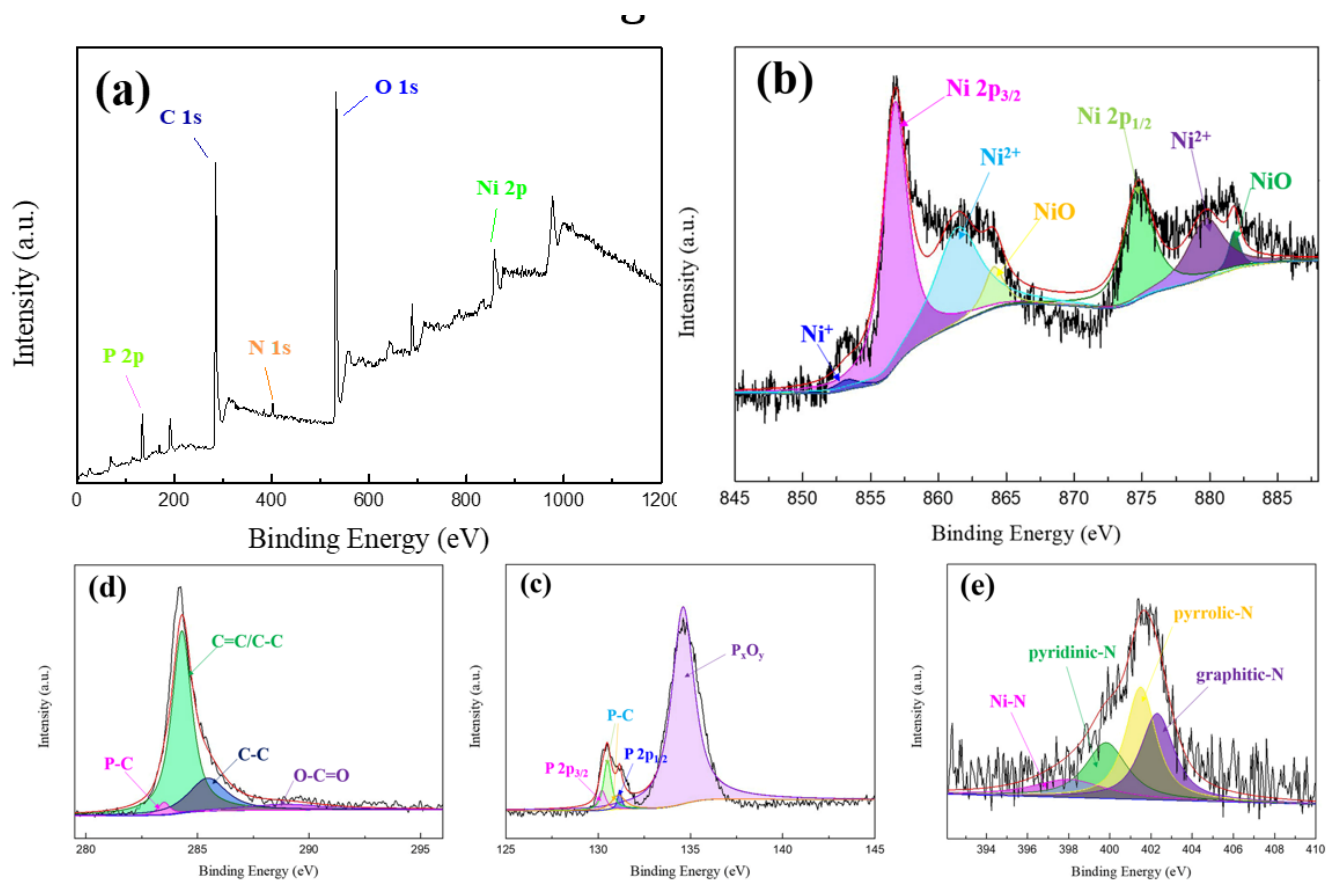
Figure 4 (a) XPS survey of Ni₃N/BP-AG-1, and high-resolution region of (b-e) Ni 2p, P 2p, C 1s and N 1s in the Ni₃N/BP-AG-1.

The *IR*-corrected linear scan voltammetry (LSV) polarization curves toward OER for catalysts have been displayed in **Figure 5**a, the prepared Ni₃N/BP-AG catalysts with different proportions of formula, Ni₃N/BP, Ni₃N/AG, and BP-AG hybrids were investigated together for comparison. The Ni₃N/BP-AG with the frequently-used mass ratio of 1: 1: 1 (Ni₃N/BP-AG-1) only demands an overpotential of ～233 mV to reach 10 mA cm⁻². While the other options require higher overpotentials for the current density of 10 mA cm⁻² (308 mV for Ni₃N/BP-AG-2, 245 mV for Ni₃N/BP-AG-0.5, 317 mV for Ni₃N/AG, 292 mV for Ni₃N/BP and 377 mV for BP-AG, severally). The overpotential for Ni₃N/BP-AG-1 was
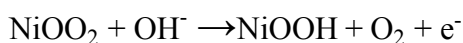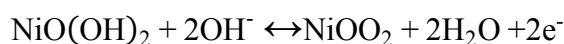
optimized and even much better than the commercial RuO_2 catalyst which needs an overpotential of more than 300 mV at the same condition. And the supererogatory expense of energy undisputed accompanied by the large overpotential. The lower overpotential is excellent among other recently reported active OER catalysts by contrast (**Figure S4** [19, 26, 34-38]).
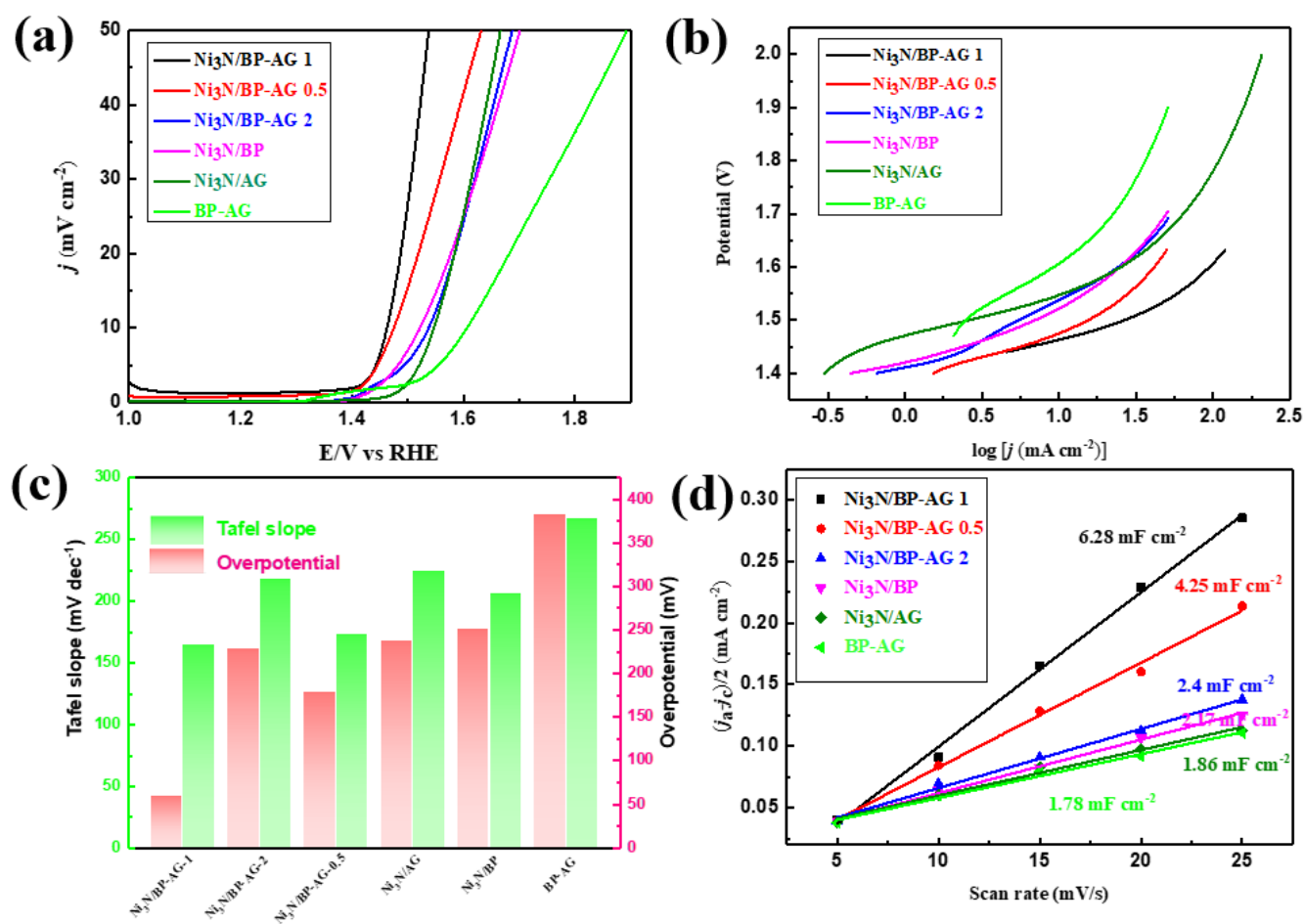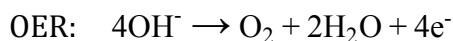

Figure 5 OER performance. (a) IR compensated polarization curves of the Ni_3N/BP-AG-2, Ni_3N/BP-AG-1, Ni_3N/BP-AG-0.5, Ni_3N/BP, Ni_3N/AG and BP-AG, scan rate: 5 mV s^{-1} (b) Tafel slopes, (c) the summarized overpotentials and Tafel plots at the 10 mA cm^{-2} and (d) Plots of the double-layer capacitances.

As a pivotal kinetic parameter, Tafel slope values are frequently used to incarnate the OER pathway and the rate-limiting step of the electrochemical behavior [39]. Therefore, a four-electron transfer process can be discovered while the mechanism of OER in alkaline solution is analyzed. Same as before, the smallest Tafel slope of 42 mV dec^{-1} belongs to Ni$_3$N/BP-AG-1 within all the options indicating a changed rate-determining step (**Figure 5**b). While the corresponding Tafel slopes of Ni$_3$N/BP-AG-2, Ni$_3$N/BP-AG-0.5, Ni$_3$N/BP, Ni$_3$N/AG, and BP-AG are calculated to 161, 126, 168, 177 and 270 mV dec^{-1}, respectively. **Figure 5**c summarizes the essential property of electrocatalysts. It is pretty evident that the Ni$_3$N/BP-AG-1 is the best in both overpotential and Tafel slope. The performance of other catalysts in this series is shown in **Figure S5**.

In contrast, the source of benign value might give credit to the surface and interface structure of compound, which keep the building steady. And the defects of nanosheets for absorbing *OH are operated successfully. Surface hydrogen/oxide complexes that are readily formed during electrolysis have been formed to be synergistic catalytically active sites for the reported nitride or phosphide OER catalysts [31]. Moreover, as previously speculated, the acceleration of the kinetics is also likely to be inseparable from the complete electron transfer channel of the catalyst. And the special interface between NiO and Ni$_3$N is conducive to form active sites with spectacular efficiency [31]. On the other hand, it is recognized that the existence of Ni^{2+} which could be further oxidized to NiOOO* plays an important role in the catalytic process [19, 23].

$$Ni^{2+} + 3OH^- \leftrightarrow NiOOH + H_2O + e^-$$

$$NiOOH + OH^- \leftrightarrow NiO(OH)_2 + e^-$$

$$NiO(OH)_2 + 2OH^- \leftrightarrow NiOO_2 + 2H_2O + 2e^-$$

$$NiOO_2 + OH^- \rightarrow NiOOH + O_2 + e^-$$

$$\text{OER:} \quad 4OH^- \rightarrow O_2 + 2H_2O + 4e^-$$

To further understand the mechanism of OER in the Ni^{2+} sites, four basic steps which had been explored by previous researchers can be described as shown above [23]. In the beginning, the Ni^{2+} combines with the *OH in the electrolyte to form the NiOOH. Then, the NiOOH further reacts with the *OH. As a result, the NiOOO* integrates with the *OH in the third step. In this step, the $NiOO_2$ and H_2O will be fabricated simutanuously. Finally, the $NiOO_2$ acts with the *OH again to finish the process of four-step electron transfer. The first three steps identify the rate of all OER. Particularly, the simultaneous regeneration of NiOOH is accompanied by the formation of oxygen. That means partial energy barrier of reaction may be reduced in the next courses. Thus, the excellent property of Ni_3N/BP-AG-1 for OER may be explained.

The effective electrochemical active surface area (ECSA) of catalysts was investigated in **Figure 5**d for interpretation of the improved OER performance pertain to Ni_3N/BP-AG-1 by estimating the double-layer capacitance (C_{dl}) on the basis of the cyclic voltammetry (CV) results at different scan rates. As can be seen from the illustration, the capacitance from Ni_3N/BP-AG-1 electrode reaches up to 6.28 mF cm^{-2}. This value greatly exceeds the second value of 4.25 mF cm^{-2} (Ni_3N/BP-AG-0.5), which suggests that Ni_3N/BP-AG-1 shows the most effective active sites. Further, electrochemical impedance spectroscopies (EIS) of catalysts are investigated **(Figure S6**a). The classic Nyquist plots show the diameter of the semicircles diminution, manifesting that Ni_3N/BP-AG-1 has the fastest electron transfer [32]. Therefore, it is obvious that the active surface of the catalytic reaction is more readily available according to the above nanostructure evolution [8, 40]. Corresponding to the respond of Raman analysis, the intrinsic excellent catalytic behavior of the Ni_3N/BP-AG-1 can be derived from this side. Lifted edges and defects facilitate the full contact of the active sites with the electrolyte, which will be attributed to the establishment of a stable heterojunction

substrate of BP-AG with a special structure due to the high temperature and high pressure in the ball milling process.
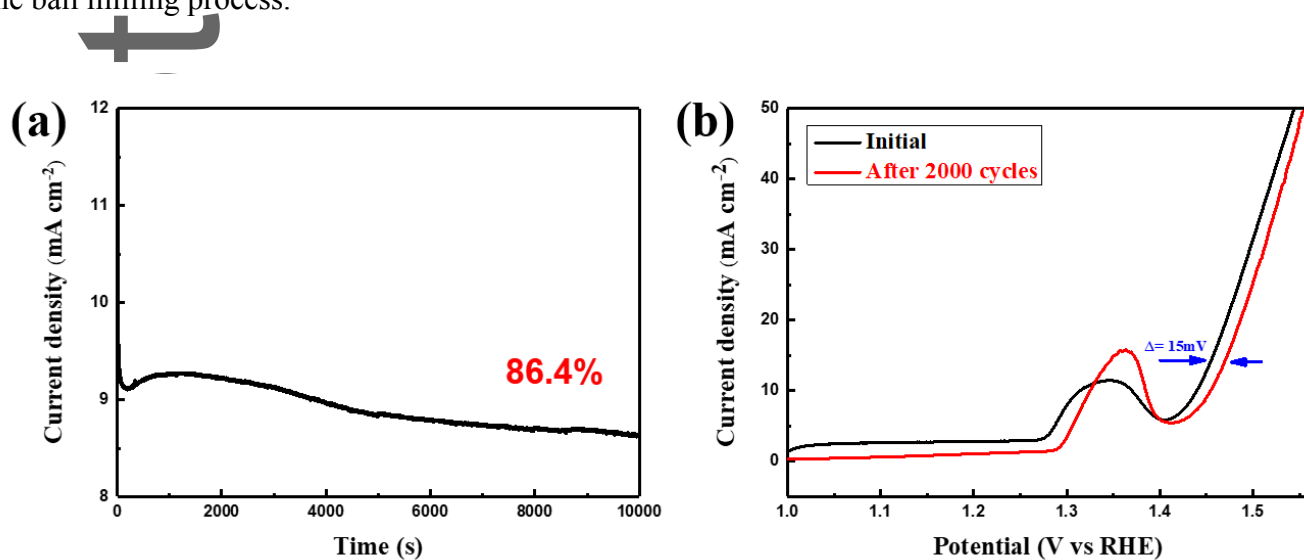
Figure 6 (a) I-t curve obtained for OER with the Ni_3N/BP-AG-1 at 233 mV and(b) Polarization curves of the Ni_3N/BP-AG-1 recorded before and after 2000 cycles, scan rate: 50mV s^{-1}.

Furthermore, the superior activity of Ni_3N/BP-AG-1 can be understood via examinations of stability and durability. Here, in **Figure 6**a, Ni_3N/BP-AG-1 is evaluated by chronoamperometry in the 1 M KOH solution with a constant potential of 233 mV which is equal to the overpotential. The curve that symbolized the alteration of current density along with reaction time basically remained unchanged after a 10000 s long continuous operation. It is noting that there is a transitory process of current density dropping that appeared at the beginning of durability tests. The deactivation of current density might charge upon the oxidation on the surface of the partial BP component, which would be contaminated readily under the oxygen-enriched condition. Even then, the Ni_3N/BP-AG-1 catalyst still shows good electrochemical durability. The initial current density remains over 86.4% after 10000 s, which is better than other ratios (**Figure S6**b). Moreover, the stability of the as-prepared Ni_3N/BP-AG-1 is illustrated in **Figure 6**b. After 2000 continuous CV cycles at a scanning

rate of 50 mV s^{-1}, negligible activity loss about 15 mV was observed, further confirming its possibility of widespread application.

All tests prove that the ratio of 1: 1: 1 is optimal among three projects, which might attribute to the best retention of Ni$_3$N during the ball milling process. By contrast, the representative peak located at 853.2 eV cannot be clearly observed in both Ni$_3$N/BP-AG-2 and Ni$_3$N/BP-AG-0.5, particularly on the latter **(Figure S7**a, b). Unusually, the peaks around 870.9 eV can be consistent with the high-resolution Ni 2p spectra of Ni$_3$N/BP-AG-2, which is identified the symbol of metal Ni. Hence, partial Ni$_3$N particles might be reduced to metal Ni because of the high pressure and temperature, which were generated by the drastic impact. And this impact may induce the fracture of Ni-N bonds or the phase transformation which resulted in unremarkable electrocatalytic performances of Ni$_3$N/BP-AG-2. And the TEM images (**Figure S8**a, b) of Ni$_3$N/BP-AG-2 coordinated with the XPS analysis. According to **Figure S8**, the sporadic Ni$_3$N particles were disappeared and substituted by a wide range of black bulk. And the entire area became almost opaque. In **Figure S8**c, partial Ni$_3$N particles of Ni$_3$N/BP-AG-0.5 are aggregated. As is known to all, the generation of unsaturated active sites might be fabricated in the course of mechanical exfoliation due to the amplifying defects of BP. Thus, the electrocatalytic performances of Ni$_3$N/BP-AG-2 with skimp effective active sites have nothing on Ni$_3$N/BP-AG-1.

3 Conclusion

In summary, the Ni$_3$N supported on BP-AG heterostructure hybrids as an easy to implement and low-cost electrocatalyst for OER was successfully fabricated. Firstly, the steady BP-AG heterostructure depends on the strong P-C bonds was gained via a handy mechanical ball milling method. The formation of Ni-P bonds reflected the junction between metal and semiconductor might dramatically improve the reaction rate. And because of the Ni atoms partially oxidized, the nice activity of Ni$_3$N/BP-AG-1 may be ascribed to the formation of NiOOH layers in OER process and the special interface between NiO and Ni$_3$N. The

as-prepared Ni$_3$N/BP-AG-1 exhibited agreeable electrocatalytic activity for OER in alkaline condition. The Ni$_3$N/BP-AG-1 electrode was able to risk a current density of 10 mA cm^{-2} at overpotentials of 233 mV. Similarly, Tafel slope of 42 mV dec^{-1} was far lower than that of the commercial noble metal catalyst, too. In addition, the doping effect of N atoms cannot be ignored. What is noteworthy is that the property of Ni$_3$N/BP-AG-1 is the best just at present, while that of Ni$_3$N/BP-AG-0.5 is nearby. Considering this aspect, the existence of more satisfying synthesis recipe may be verified in the near future. Therefore, a lot of windows could be the next door to further enhance the utility value of Ni$_3$N/BP-AG hybrids.

4 Experimental Section

4.1 Chemicals

Graphene powder (Physical methods, Size: 0.5~5 μm, Thickness: 1~2 nm, Single-layer ratio: ~80%) were purchased from Nanjing XFNANO Materials Tech Co., Ltd. Red phosphorus (99.999% metals basis,1-5mm). Nickel chloride hexahydrate (99.999% metals basis). Nafion solution (5 wt%) was purchased from Shanghai Geshi Energy Technology Co., Ltd. Isopropyl Alcohol (GC, ≥99.9%). The chemicals are all used as obtained without any purification.

4.2 Material Synthesis

4.2.1 Preparation of BP nanosheets

BP was obtained via straightway ball-milling red phosphorus (RP) under an argon atmosphere. Briefly, 2 g of RP was added into a 25 mL Teflon-lined stainless-steel autoclave with 17.5 mL of deionized water (DI). Then, the hydrothermal process occurred at 180 °C for 20 hours to remove the surface oxidation drastically. Followed, the dry RP particles were ground into a pristine powder. Followed, about 1.6 g of the surplus pristine RP powder and number of stainless-steel balls which contain different specifications were added into a

stainless-steel jar with a capacity of 50 cm^3. The ball milling project has proceeded under an argon-saturated condition for 48 hours with a rotation speed of 500 r min^{-1}. Peculiarly, the transformed BP was keeping under the argon protection for later use.

4.2.2 Activation of commercial pristine graphene nanosheets

AG was produced from the etched graphene powder. At first, the graphene powder was submerged in 60 mL of 6 M KOH aqueous solution and stirred for 12 hours to ensure the full contact between graphene and background. Next, the graphene was centrifuged and dried in a vacuum oven at 70 °C overnight. After simple trituration, the graphene was treated at 800 °C for two hours with the heating rate of 2 °C min^{-1} under flowing N$_2$ gas. And then, the graphene was naturally cooled to room temperature.

4.2.3 Synthesis of Ni$_3$N particles

In the beginning, 0.594 g of NiCl$_2$•6H$_2$O, 0.185 g of NH$_4$F and 0.75 g of urea were dissolved in 70 mL DI. In the next, the mixed solution was transferred into a 100 mL Teflon-lined stainless-steel autoclave and subjected to hydrothermal reaction conditions at 120 °C for 4 hours to form the procedure. The product was separated by centrifugation and washed with DI and ethanol for several times. Afterwards, the procedure was dried in a vacuum oven at 80 °C for 12 hours. The collected solid powder was then placed in a tube furnace and heated to 250 °C for 2 hours under air. Finally, the procedure was maintained in NH$_3$ atmosphere and heated to 380 °C for 2 hours.

4.2.4 Fabrication of BP-AG and Ni$_3$N/BP-AG

For fabricating the BP-AG, 100 mg of BP, 100 mg of AG and appropriate balls were throwed into the jar that as same as the jar used in previously experiment. At the same time, the argon gas enclosed unremittingly into the jar to protect the BP nanosheets for 30 minutes.

After milling for 48 hours with a rotation speed of 800 r min^{-1}, the BP-AG compounds were conserved in the jar with engorged argon gas.

Furthermore, the Ni$_3$N/BP-AG with different synthesis formula could be obtained via changing the additive mass of Ni$_3$N. Herein, 200 mg, 100 mg and 50 mg of as-prepared Ni$_3$N were added into jars (800 r min^{-1}, 48 h), respectively. At last, the Ni$_3$N/BP-AG-2, Ni$_3$N/BP-AG-1 and Ni$_3$N/BP-AG-0.5 were gained and storage in the argon-saturated bottle.

4.3 Electrocatalytic measurement

The electrochemical tests of the samples were evaluated in a typical three-electrode systems on a CHI660E electrochemical workstation. The prepared catalysts were directly used as a working electrode. A graphite rod electrode and an Ag/AgCl electrode were used as the counter electrode (CE) and reference electrode (RE), respectively. All samples were prepared by adding 5 mg of the catalyst into 1 ml of solution which consist of 800 μL of isopropyl alcohol, 170 μL of H$_2$O and 30 μL of 5% Nafion solution, followed by ultrasonication for 1 hours to form the homogeneous inks. Then, 10 μL of sample ink was warily dropped onto the smooth glassy carbon rotating disk electrode (RDE). The LSV and stabilization tests were investigated in O$_2$-saturated 1.0 M KOH.

4.4 Material Characterization

XRD characterization data were collected by using a Bruker D8 advance. Raman spectrum was carried out on a Thermo ESCALAB 250 system with a LabRAM HR Evolution (λ=633 nm). TEM images were gained on a JEOL JEM-2100F. AFM images were measured by an Agilent 5500AFM. XPS measurements were performed on a Kratos Axis UltraDLD with Al-Kα X-ray (1486.6 eV) radiation.

Acknowledgements

Conflict of Interest

The authors declare no conflict of interest.

References

[1] Zhang, Z.; Zhou, D.; Liao, J.; Bao, X.; Yu, H., *Int J Energy Res.* **2019,** *43*, 1460.

[2] Xie, Z.; Tang, H.; Wang, Y., *ChemElectroChem* **2019,** *6*, 1206.

[3] Gong, Y.; Xu, Z.; Pan, H., *ChemistrySelect* **2019,** *4*, 1131.

[4] Zhu, J.; Yang, D.; Yin, Z.; Yan, Q.; Zhang, H., *Small* **2014,** *10*, 3480.

[5] Wang, M.; Lin, M.; Li, J.; Huang, L.; Zhuang, Z.; Lin, C.; Zhou, L.; Mai, L., *Chem Commun (Camb)* **2017,** *53*, 8372.

[6] Fan, Y.; Ida, S.; Staykov, A.; Akbay, T.; Hagiwara, H.; Matsuda, J.; Kaneko, K.; Ishihara, T., *Small* **2017,** *13*, 1700099.

[7] Feng, L. L.; Li, G. D.; Liu, Y.; Wu, Y.; Chen, H.; Wang, Y.; Zou, Y. C.; Wang, D.; Zou, X., *ACS Appl. Mater. Interfaces* **2015,** *7*, 980.

[8] Su, J.; Li, G.-D.; Li, X.-H.; Chen, J.-S., *Adv. Sci.* **2019**, 1801702.

[9] Ren, X.; Zhou, J.; Qi, X.; Liu, Y.; Huang, Z.; Li, Z.; Ge, Y.; Dhanabalan, S. C.; Ponraj, J. S.; Wang, S.; Zhong, J.; Zhang, H., *Adv. Energy Mater.* **2017,** *7*, 1700396.

[10] Wang, J.; Liu, D.; Huang, H.; Yang, N.; Yu, B.; Wen, M.; Wang, X.; Chu, P. K.; Yu, X. F., *Angew. Chem. Int. Ed.* **2018,** *57*, 2600.

[11] Wu, R. J.; Topsakal, M.; Low, T.; Robbins, M. C.; Haratipour, N.; Jeong, J. S.; Wentzcovitch, R. M.; Koester, S. J.; Mkhoyan, K. A., *J. Vac. Sci. Technol. A* **2015,** *33*, 060604.

[12] Li, L.; Yu, Y.; Ye, G. J.; Ge, Q.; Ou, X.; Wu, H.; Feng, D.; Chen, X. H.; Zhang, Y., *Nat. Nanotechnol.* **2014,** *9*, 372.

[13] Gusmão, R.; Sofer, Z.; Pumera, M., *Angew. Chem. Int. Ed.* **2017,** *56*, 8052.

[14] Liu, H.; Du, Y.; Deng, Y.; Ye, P. D., *Chem. Soc. Rev.* **2015,** *44*, 2732.

[15] Shen, Z.; Sun, S.; Wang, W.; Liu, J.; Liu, Z.; Yu, J. C., *J. Mater. Chem. A* **2015,** *3*, 3285.

[16] Zhu, M.; Kim, S.; Mao, L.; Fujitsuka, M.; Zhang, J.; Wang, X.; Majima, T., *J. Am. Chem. Soc.* **2017,** *139*, 13234.

[17] Jiang, Q.; Xu, L.; Chen, N.; Zhang, H.; Dai, L.; Wang, S., *Angew. Chem. Int. Ed.* **2016,** *55*, 13849.

[18] Gao, D.; Zhang, J.; Wang, T.; Xiao, W.; Tao, K.; Xue, D.; Ding, J., *J. Mater. Chem. A* **2016,** *4*, 17363.

[19] Liu, T.; Li, M.; Jiao, C.; Hassan, M.; Bo, X.; Zhou, M.; Wang, H.-L., *J. Mater. Chem. A* **2017,** *5*, 9377.

[20] Nandi, S.; Singh, S. K.; Mullangi, D.; Illathvalappil, R.; George, L.; Vinod, C. P.; Kurungot, S.; Vaidhyanathan, R., *Adv. Energy Mater.* **2016,** *6*, 1601189.
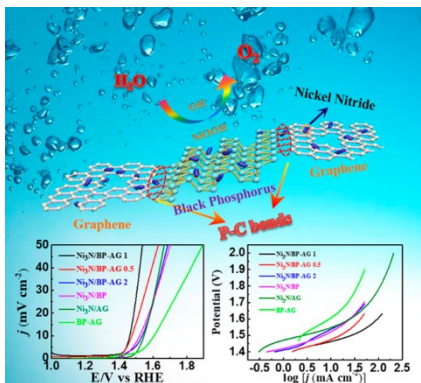
[21] Han, L.; Feng, K.; Chen, Z., *Energy Technol.* **2017,** *5*, 1908.

[22] Wu, T.; Ma, Y.; Qu, Z.; Fan, J.; Li, Q.; Shi, P.; Xu, Q.; Min, Y., *ACS Appl. Mater. Interfaces* **2019,** *11*, 5136.

[23] Xu, K.; Chen, P.; Li, X.; Tong, Y.; Ding, H.; Wu, X.; Chu, W.; Peng, Z.; Wu, C.; Xie, Y., *J. Am. Chem. Soc.* **2015,** *137*, 4119.

[24] Wu, T.; Fan, J.; Li, Q.; Shi, P.; Xu, Q.; Min, Y., *Adv. Energy Mater.* **2018,** *8*, 1701799.

[25] Abellan, G.; Wild, S.; Lloret, V.; Scheuschner, N.; Gillen, R.; Mundloch, U.; Maultzsch, J.; Varela, M.; Hauke, F.; Hirsch, A., *J. Am. Chem. Soc.* **2017,** *139*, 10432.

[26] Shi, F.; Geng, Z.; Huang, K.; Liang, Q.; Zhang, Y.; Sun, Y.; Cao, J.; Feng, S., *Adv. Sci.* **2018,** *5*, 1800575.

[27] Crowther, A. C.; Ghassaei, A.; Jung, N.; Brus, L. E., *ACS Nano* **2012,** *6*, 1865.

[28] Hassoun, J.; Bonaccorso, F.; Agostini, M.; Angelucci, M.; Betti, M. G.; Cingolani, R.; Gemmi, M.; Mariani, C.; Panero, S.; Pellegrini, V.; Scrosati, B., *Nano Lett.* **2014,** *14*, 4901.

[29] Zhu, M.; Sun, Z.; Fujitsuka, M.; Majima, T., *Angew. Chem. Int. Ed.* **2018,** *57*, 2160.

[30] Stern, L.-A.; Feng, L.; Song, F.; Hu, X., *Energy Environ. Sci.* **2015,** *8*, 2347.

[31] Huang, J.; Sun, Y.; Du, X.; Zhang, Y.; Wu, C.; Yan, C.; Yan, Y.; Zou, G.; Wu, W.; Lu, R.; Li, Y.; Xiong, J., *Adv. Mater.* **2018,** *30*, 1803367.

[32] Lu, X.; Gu, L.; Wang, J.; Wu, J.; Liao, P.; Li, G., *Adv. Mater.* **2017,** *29*, 1604437.

[33] Bai, X.; Wang, Q.; Xu, G.; Ning, Y.; Huang, K.; He, F.; Wu, Z. J.; Zhang, J., *Chem. Eur. J.* **2017,** *23*, 16862.

[34] Sun, Y.; Zhang, T.; Li, X.; Bai, Y.; Lyu, X.; Liu, G.; Cai, W.; Li, Y., *Adv. Mater. Interfaces* **2018,** *5*, 1800473.

[35] Ding, D.; Shen, K.; Chen, X.; Chen, H.; Chen, J.; Fan, T.; Wu, R.; Li, Y., *ACS Catal.* **2018,** *8*, 7879.

[36] Pan, Y.; Sun, K.; Liu, S.; Cao, X.; Wu, K.; Cheong, W. C.; Chen, Z.; Wang, Y.; Li, Y.; Liu, Y.; Wang, D.; Peng, Q.; Chen, C.; Li, Y., *J. Am. Chem. Soc.* **2018,** *140*, 2610.

[37] Wang, N.; Li, L.; Zhao, D.; Kang, X.; Tang, Z.; Chen, S., *Small* **2017,** *13*, 1701025.

[38] Shi, Y.; Yu, Y.; Liang, Y.; Du, Y.; Zhang, B., *Angew. Chem. Int. Ed.* **2019,** *58*, 3769.

[39] Stevens, M. B.; Enman, L. J.; Batchellor, A. S.; Cosby, M. R.; Vise, A. E.; Trang, C. D. M.; Boettcher, S. W., *Chem. Mater.* **2016,** *29*, 120.

[40] Wu, A.; Xie, Y.; Ma, H.; Tian, C.; Gu, Y.; Yan, H.; Zhang, X.; Yang, G.; Fu, H., *Nano Energy* **2018,** *44*, 353.

Summary of the Article

The black phosphorus (BP)-activated graphene (AG) heterostructure is designed for supporting nickel nitride (Ni_3N) to enhance the performance of oxygen evolution reaction (OER). The Ni_3N/BP-AG exhibits excellent electrocatalytic performance toward OER with low overpotential 233 mV to achieve a catalytic current density of 10 mA cm^{-2} and small Tafel slope of 42 mV dec^{-1}. It also shows remarkable stability with a retention rate of ~ 86.4% OER activity after 10,000 s.